01,03

# Electronic structure and X-ray spectral characteristics of the semiconductor and metal phases of iron disilicide

© G.P. Potudanskii, S.I. Kurganskii

Voronezh State University,
Voronezh, Russia

E-mail: potudanskiy@phys.vsu.ru

Received September 12, 2022
Revised September 12, 2022
Accepted September 16, 2022

Within the framework of the full-potential method of augmented plane waves with local orbitals, the electronic structure and X-ray spectral characteristics of the semiconductor and metal phases of iron disilicide were calculated. The total and partial densities of electronic states, the band structure, and X-ray absorption spectra of the iron *K*-edge were calculated. The results are compared with the known experimental data. An explanation is given of the change in the X-ray absorption near edge structure during the transition from the semiconductor phase to the metallic one.

**Keywords:** iron disilicide, electronic structure, APW+lo, method, XANES, *K*-edge.

DOI: 10.21883/PSS.2023.01.54967.474

## 1. Introduction

Currently, with the development of nanoelectronics and spintronics, there is interest in fundamental and applied research [1,2], which entails the need for high-precision methods for analyzing the physicochemical properties of materials. The nanostructures made of transition metal disilicides are one of the fundamental materials in the production of micro- and nanoelectronics [3,4]. Among these compounds, iron disilicide [5,6] is of particular interest, since it is capable of forming metallic and semiconductor phases. The densities of electronic states and the band structure play an important role in predicting various properties of materials, including quantum ones. It is known that reducing the size of crystals to the nanometer scale causes a change in properties at the interface [6,7]. Therefore, a comprehensive study of $FeSi_2$ is of fundamental importance. In the work [8], they obtained the spectra of the X-ray absorption near edge structure spectroscopy (XANES), near the *K*-edges of iron absorption in the multilayered nanostructure, consisting of layers of magnetic transition metals $Co_{45}Fe_{45}Zr_{10}$, separated by non-magnetic layers consisting of $SiO_2$ and *a*-Si. The discovered identity of these spectra and the spectrum of the *K*-absorption edge of metallic iron turned out to be completely unexpected and necessitates an explanation of this fact. We perform calculations $FeSi_2$ in order to further determine whether this compound is present in these multilayer nanostructures at interlayer boundaries, since in the work [8] the main maximum of the absorption *K*-edge is located at the same distance from the absorption edge as for iron silicides.

Previously, iron disilicide has already been partially investigated, for example, in the works [9–11], the study of the band structure of only the metal phase $\alpha$-$FeSi_2$ was carried out, while in the work [12], the study of already both phases, and in the works [13–17], only $\beta$-$FeSi_2$ was studied. It should be noted that in the works of [12,14], the energy gaps in the band structure of the semiconductor phase turned out to be direct, and in [13,16] — indirect and the position of the extremes coincided.

The difference in the band structures obtained in different calculations can be explained by the use of different theoretical methods, which are improved over time. Experimental methods are also being improved over time, for example, in the works of [18,19] on the absorption spectra of iron, an increase in broadening with an increase in energy can be noticed, leading to the fact that the main maximum, which, as we will show below, is double, becomes single in the experiment and is not suitable for use in works where a higher resolution is required. The current development of machine learning methods [20] can make it possible to determine which compounds are present at the boundaries of the multilayered nanostructures, and the use of spectra in higher resolution can have a significant impact.

Therefore, the aim of this work is an unambiguous theoretical determination of the electronic structure of the semiconductor and metallic phases of iron disilicide, in particular, the transformation of the *K*-edge of iron absorption during the transition from the semiconductor phase to the metallic one.

## 2. Calculation method

As part of the density functional theory (DFT), calculations of the electronic structure of the semiconductor and metallic phases of iron disilicide were carried out in the quantum mechanical software package Wien2k [21], which

is based on both the full-potential method of linearized augmented plane waves (FP-LAPW) and the full-potential augmented plane wave plus local orbitals (FP-APW+lo) [22]. The FP-APW+lo method allows obtaining more accurate electric field gradients (EFG), eliminating the appearance of so-called phantom bands and providing better convergence of the Self-Consistent cycle (SCF) for atoms that have semicore states, unlike FP-LAPW[23].

The FP-APW+lo method allows obtaining more accurate electric field gradients (EFG), eliminating the appearance of so-called phantom bands and providing better convergence of the Self-Consistent cycle (SCF) for atoms that have semicore states, unlike FP-LAPW [23].

The calculation of the metal $FeSi_2$ was carried out by the bulk method FP-APW+lo with an exchange-correlation functional in the approximation of the generalized gradient approximation (PBE-GGA) [24], which, as we previously showed [25], allows you to get a reliable result when calculating the electronic structure of bulk crystals and nanofilms. The calculation of the semiconductor $FeSi_2$ was carried out by the same method FP-APW+lo, but with a functional in the approximation of the modified Becky–Johnson exchange-correlation potential (mBJ-LDA) [26], which allows us to obtain a more accurate value of the width the band gap of semiconductors and dielectrics [27].

To calculate the densities of electronic states and band structures in the ground state, ordinary unit cells and 10000**k**-vectors in the first Brillouin zone were used. To calculate the electronic structure in the excited state, which is necessary for the correct description of the XANES spectra, a supercell and 200**k**-vectors in the first Brillouin zone were used. The parameter $r_{mt}k_{\max}$, which determines the number of basis functions, was taken to be 6, where $r_{mt}$ — the smallest of the radii of muffin-tin spheres, $k_{\max}$ — the boundary of the breakage of the augmented waves. The Self-Consistent cycle is performed until the change in total energy between two consecutive iterations becomes sufficiently small.

## 3. Calculation details

Iron disilicide exists in two phases: low-temperature (luobusaite) and high-temperature (linzhiite) [28]. At atmospheric pressure, luobusaite is stable up to 1243 K. When the temperature rises, luobusaite begins to form linzhiite by peritectic formation with iron silicide ($\alpha$-$Fe_{0.92}Si_2$), which is stable up to the melting point, which is 1489 K. When the temperature of linzhiite decreases to 1188 K, the eutectoid transformation into silicon and luobusaite begins ($\beta$-$FeSi_2$) [28].

The linzhiite ($\alpha$-$FeSi_2$ or $\alpha$-$Fe_{0.92}Si_2$) — metal, belongs to tetragonal symmetry, has a spatial symmetry group *123_P4/mmm* and an unit cell with parameters $a = 2.6840$ Å, $b = 2.6840$ Å, $c = 5.1280$ Å, which contains 1 formula unit. The coordinates of the atoms in the unit cell are given in Table. 1 [29]. This phase has another name — $\alpha$-leboite [30]. Some researchers call this phase $\xi$-$FeSi_2$ [28].

**Table 1.** Coordinates of atoms $\alpha$-$FeSi_2$ [29]

| Atom | $X/a$ | $Y/b$ | $Z/c$ |
|---|---|---|---|
| Si | 1/2 | 1/2 | 0.2700 |
| Si | 1/2 | 1/2 | 0.7300 |
| Fe | 0 | 0 | 0 |

**Table 2.** Coordinates of atoms $\beta$-$FeSi_2$ [31]

| Atom | $X/a$ | $Y/b$ | $Z/c$ |
|---|---|---|---|
| Si1 | 0.1282 | 0.2746 | 0.0512 |
| Si1 | 0.8718 | 0.7254 | 0.9488 |
| Si1 | 0.1282 | 0.7746 | 0.4488 |
| Si1 | 0.8718 | 0.2254 | 0.5512 |
| Si1 | 0.8718 | 0.2746 | 0.0512 |
| Si1 | 0.1282 | 0.7254 | 0.9488 |
| Si1 | 0.8718 | 0.7746 | 0.4488 |
| Si1 | 0.1282 | 0.2254 | 0.5512 |
| $Si_2$ | 0.1273 | 0.0450 | 0.2739 |
| $Si_2$ | 0.8727 | 0.9550 | 0.7261 |
| $Si_2$ | 0.1273 | 0.5450 | 0.2261 |
| $Si_2$ | 0.8727 | 0.4550 | 0.7739 |
| $Si_2$ | 0.8727 | 0.0450 | 0.2739 |
| $Si_2$ | 0.1273 | 0.9550 | 0.7261 |
| $Si_2$ | 0.8727 | 0.5450 | 0.2261 |
| $Si_2$ | 0.1273 | 0.4550 | 0.7739 |
| Fe1 | 0.2146 | 0 | 0 |
| Fe1 | 0.7854 | 0 | 0 |
| Fe1 | 0.2146 | 0.5 | 0.5 |
| Fe1 | 0.7854 | 0.5 | 0.5 |
| Fe2 | 0 | 0.3086 | 0.3149 |
| Fe2 | 0 | 0.6914 | 0.6851 |
| Fe2 | 0 | 0.8086 | 0.1851 |
| Fe2 | 0 | 0.1914 | 0.8149 |

Luobusaite ($\beta$-$FeSi_2$) — is a semiconductor, it belongs to the orthorhombic syngony, has a spatial symmetry group *64_Cmca*, an unit cell with parameters $a = 9.8789$ Å, $b = 7.8038$ Å, $c = 7.4808$ Å, which contains 8 formula units. The coordinates of the atoms of the unit cell are given in Table. 2 [31].

An experimental investigation of the energy structure above the Fermi level can be carried out using the XANES spectroscopy. To simulate the XANES spectra, it is necessary to perform a band calculation for the structure in the excited state [32]. To transfer the structure to an excited state, a core hole is created and one electron is added to the conduction band to preserve electroneutrality. To exclude the interaction of neighboring excited atoms, a supercell is created with a volume larger than an unit cell. The size of the supercell is selected in such a way that the calculations for two consecutive increases of the supercell coincide with each other. To calculate the *K*-edges of XANES, a core hole was created at the

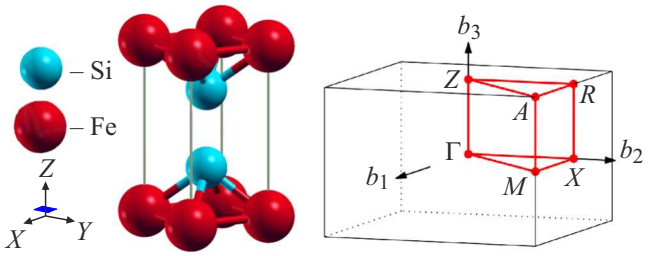


**Figure 1.** An unit tetragonal primitive cell of the Bravais lattice $\alpha$-$FeSi_2$ and the first Brillouin zone $\alpha$-$FeSi_2$ [34]. The red line indicates the path of traversing the irreducible part of the Brillouin zone when calculating the band structure.

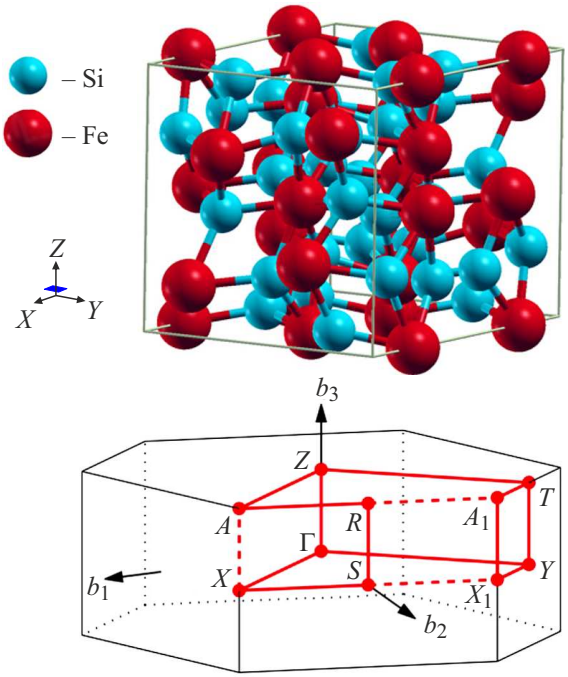


**Figure 2.** Unit rhombic base-centered Bravais lattice cell $\beta$-$FeSi_2$ and the first Brillouin zone $\beta$-$FeSi_2$ [34]. The red line indicates the path of traversing the irreducible part of the Brillouin zone when calculating the band structure.

1s-level, according to the measurement mechanism of the *K*-edges of XANES, where the core electrons, absorbing a beam of high-energy photons, are knocked out from the 1s-level.

Fig. 1, 2 show the structures $\alpha$-$FeSi_2$ and $\beta$-$FeSi_2$ and their first Brillouin zones, respectively. Visualization of the structures was carried out using the program XCrySDen [33].

## 4. Results and discussion

### 4.1. Band structure

The spectra of the total and local partial densities of electronic states obtained on the basis of the band calculation for the ground state $\alpha$-$FeSi_2$ and $\beta$-$FeSi_2$ are shown in Fig. 3, 4 respectively. The width of the valence band $\alpha$-$FeSi_2$, the minimum of which falls on the point Γ, was 14.00 eV. The magnetic moment of $\alpha$-$FeSi_2$ is missing, which is consistent with the results of our earlier calculation [35]. The estimated width of the band gap for indirect transitions $\beta$-$FeSi_2$ was 0.78 eV, for direct transitions — 0.83 eV, which corresponds to the hundredths of the values given in the Table 3 experimental values [36,37] and means that the semiconductor is indirect-gap [38].

The estimated width of the band gap for indirect transitions $\beta$-$FeSi_2$ was 0.78 eV, for direct ones — 0.83 eV, which corresponds to the hundredths of the values given in the Table. 3 experimental values [36,37] and means that the semiconductor is non-direct-band [38].

The calculated width of the valence band $\beta$-$FeSi_2$ was 13.41 eV, and its minimum is in the center (point Γ) of the first Brillouin zone. The minimum of the conduction band is in the direction of $Z$–Γ, and the maximum of the valence band is at the point $Y$, which coincides with the results of the work [13,16].

### 4.2. Density of electronic states (DOS)

Fig. 5, 6 shows the spectra of complete and local partial DOS obtained on the basis of the band calculation for the ground states $\alpha$-$FeSi_2$ and $\beta$-$FeSi_2$ respectively.

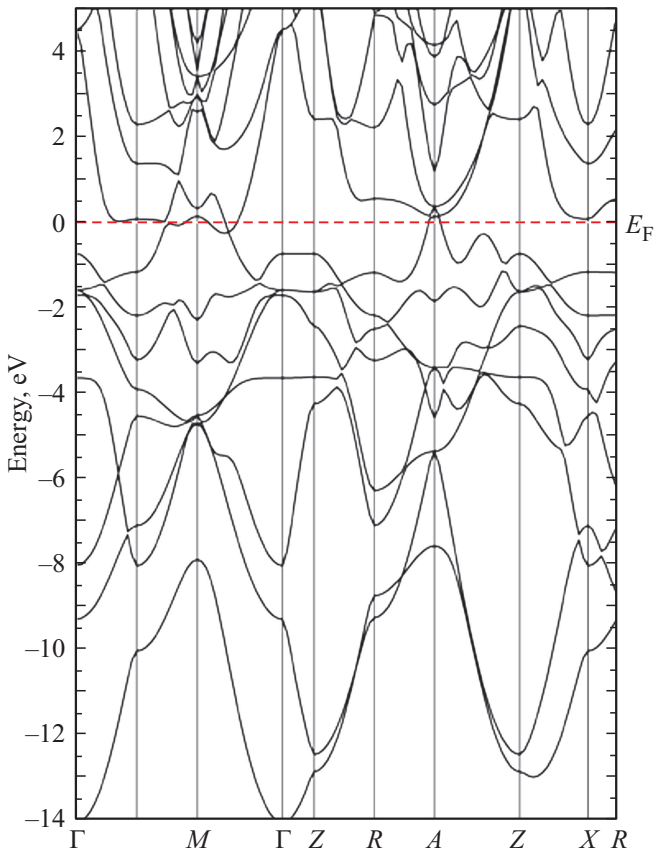


**Figure 3.** Band structure $\alpha$-$FeSi_2$.

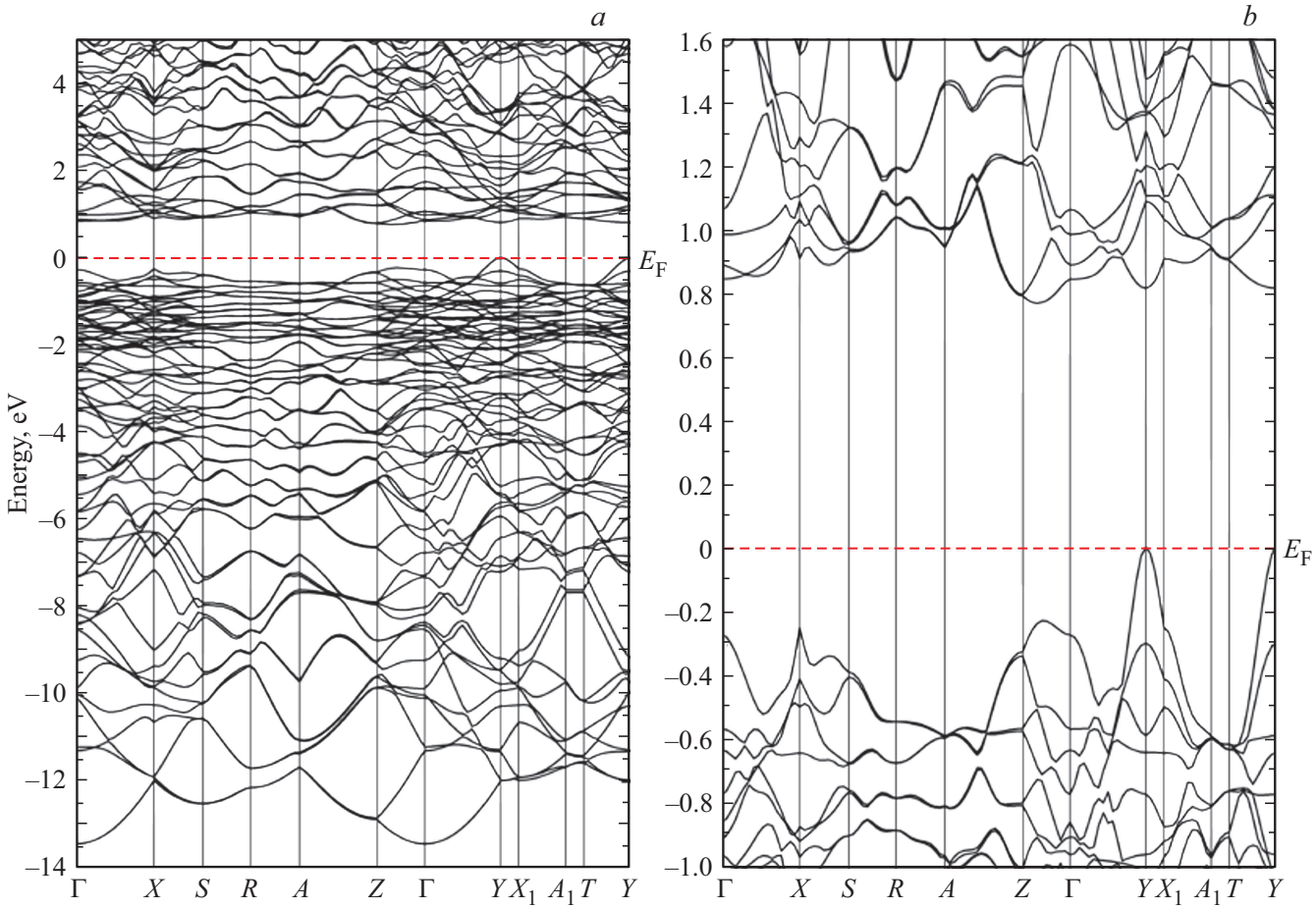


**Figure 4.** *a* — The band structure $\beta$-$FeSi_2$ in a wide energy range. *b* — band structure $\beta$-$FeSi_2$ near the Fermi level.

**Table 3.** Band gap width $\beta$-$FeSi_2$

| Source | Indirect (eV) | Direct (eV) | Temperature (K) |
|---|---|---|---|
| This study | 0.78 | 0.83 | – |
| [36] | 0.84 | 0.89 | 10 |
| [36] | 0.83 | 0.90 | 80 |
| [37] | 0.78 | 0.84 | Room |
| [37] | 0.86 | 0.875 | 77 |

The analysis of partial DOS $\alpha$-$FeSi_2$ shows that the main contribution to the Fermi region is given by *d*-iron states localized in the range from −6 to 4 eV relative to the Fermi level, in while *s*- and *p*-silicon states are predominantly localized in the ranges 5−13 eV and 1.5−7 eV is below the Fermi level. At the very same Fermi level, a minimum of both *d*-states of iron and *s*- and *p*-states of silicon was formed, which indicates that this structure can be stable.

The distribution of partial DOS $\beta$-$FeSi_2$ shows that the contribution of *s*- and *p*-states of both iron and silicon to the total DOS of the Fermi region is small, while the contribution to the valence band is made by *d*-iron states localized in the region 0−5 eV below the Fermi level and the maximum density of these states is approximately 1.5 eV below the Fermi level, and the contribution of *d*-states of the conduction band localized starting from 0.8 eV above the Fermi level and has a maximum of about 1.5 eV above the Fermi level. The distributions of *s*- and *p*-silicon states over the valence band can be characterized as follows: the highest density of *s*-states is concentrated in the region of 5−13 eV below the Fermi level, and *p*-states — in the region 0−7 eV below the Fermi level.

### 4.3. Oscillating fine structure of the X-ray absorption edge

The need for the XANES spectra simulation is due to their ability to reflect the density distribution of states contributing to the formation of the conduction band. According to the dipole selection rules, the density of *p*-states is reflected in the experimental *K*-absorption spectrum. We have calculated the specified spectrum, which was simulated using the universal PBE-GGA functional, since it allows us to obtain reliable results for both metals

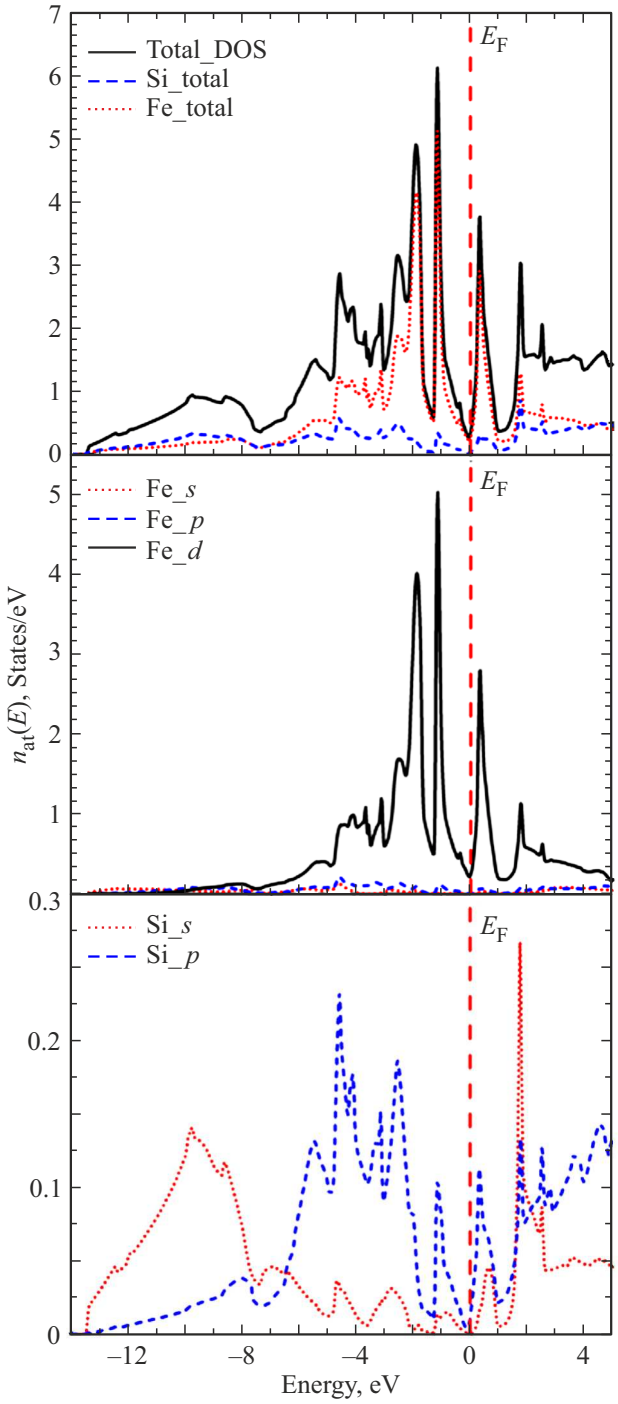


**Figure 5.** Total and partial DOS $\alpha$-$FeSi_2$.

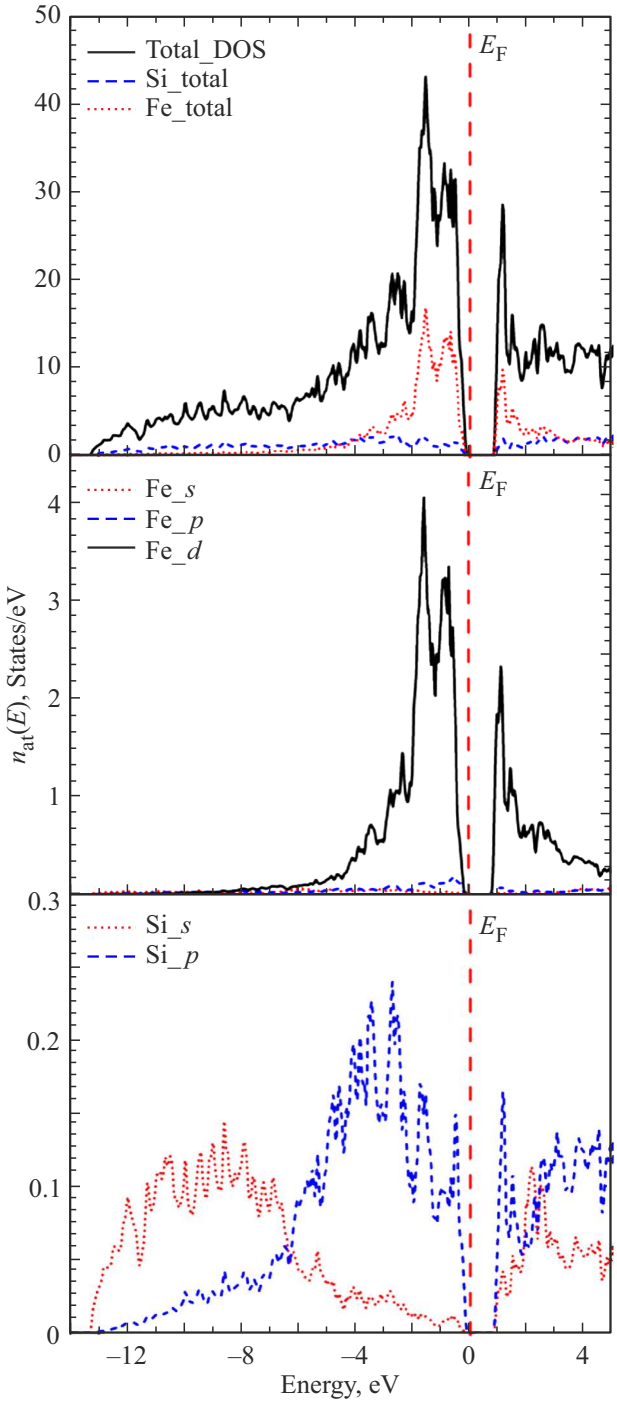


**Figure 6.** Total and partial DOS $\beta$-$FeSi_2$.

and semiconductors when calculating the XANES spectra of [39–41].

Fig. 7 shows a comparison of the experimentally registered *K*-XANES absorption edge for the semiconductor phase ($\beta$-$FeSi_2$_exp) [42], simulated for methodological purposes spectrum for this phase with very large ($\beta$-$FeSi_2$_calc(br)) and small ($\beta$-$FeSi_2$_calc) by broadening and simulated spectrum for the high-temperature metallic phase ($\alpha$-$FeSi_2$_calc). Partial *p*-states of iron DOS in the excited state in the conduction band of these phases, for which the experimentally measured Fermi level was $\sim$ 7110 eV, were compared to all spectra. The absorption edge of the semiconductor is located at an energy of $\sim$ 7110 eV, followed by a shoulder with an inflection point of $\sim$ 7114 eV, followed by a local maximum at an energy of $\sim$ 7118 eV. The double main maximum obtained in the calculation was not resolved in the experiment, which is due to the insufficient resolution of the measuring device, which we

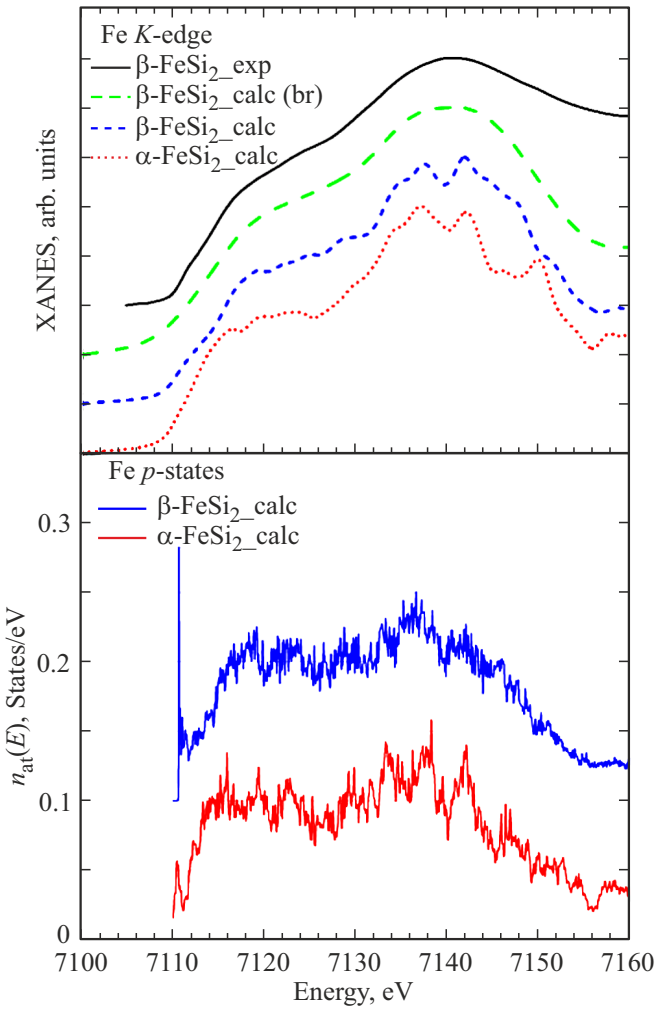


**Figure 7.** The comparison of the experimental and theoretical XANES *K*-spectra (top) $FeSi_2$ and densities *p*-states of (bottom) $FeSi_2$.

clearly show by giving the calculated spectrum with a very large broadening. The differences between the metallic phase and the semiconductor phase turned out to be as follows: the absorption edge and the shoulder shift to the Fermi level by $\sim 1$ eV, and there is also a noticeable redistribution of the intensities of two local maxima at energies $\sim 7146$ and $\sim 7150$ eV, which also shift to the Fermi level by $\sim 1$ eV. The shift of the absorption edge of the metal phase is quite an expected phenomenon, since it is a consequence of the absence of a band gap in metals. The shift of the local maxima behind the main maximum is due to the difference in the symmetry group between the two phases, since at such high energies we are dealing with another scattering mechanism — EXAFS (extended X-ray absorption fine structure), where the main contribution to absorption is given by a single scattering of a photoelectron [43,44].

## 5. Conclusion

This paper presents the results of theoretical simulation of the electronic structure of the semiconductor and metal phases of $FeSi_2$ in a wide energy domain, including the valence band and the conduction band. At the same time, there is a good agreement between the calculated spectra and the spectra obtained experimentally. The shape of the XANES *K*-edge of the iron for both phases can be considered reliably established. The results obtained in this paper will be used for further studies of the multilayered nanostructure consisting of layers of magnetic transition metals $Co_{45}Fe_{45}Zr_{10}$, separated by non-magnetic layers consisting of $SiO_2$ and *a*-Si.

### Funding

The study was carried out with the support of the Ministry of Science and Higher Education of Russia within the framework of the agreement No. 075-15-2021-1351.

### Conflict of interest

The authors declare that they have no conflict of interest.

## References

[1] V.V. Ustinov, V.B. Betelin, E.E. Tyrtyshnikov, K.V. Rudakov. Vestn. RAN **89**, *4*, 381 (2019). (in Russian).
[2] S.K. Pandey. Int. J. Sci. Studies **6**, *2*, 23 (2018).
[3] C.Y. Yang, S.M. Yang, Y.Y. Chen, K.C. Lu. Nanoscale Res. Lett. **15**, *1*, 1 (2020)
[4] G. Hamaoui, N. Horny, Z. Hua, T. Zhu, J.-F. Robillard, A. Fleming, H. Ban, M. Chirtoc. Sci. Rep. **8**, *1*, 1 (2018).
[5] J. Kalt, M. Sternik, B. Krause, I. Sergueev, M. Mikolasek, D. Bessas, O. Sikora, T. Vitova, J. Göttlicher, R. Steininger, P.T. Jochym, A. Ptok, O. Leupold, H.-C. Wille, A.I. Chumakov, P. Piekarz, K. Parlinski, T. Baumbach, S. Stankov. Phys. Rev. B **101**, *16*, 165406 (2020).
[6] S. Liang, R. Islam, D.J. Smith, P.A. Bennett. J. Cryst. Growth **295**, *2*, 166 (2006).
[7] J. Kalt, M. Sternik, I. Sergueev, J. Herfort, B. Jenichen, H.-C. Wille, O. Sikora, P. Piekarz, K. Parlinski, T. Baumbach, S. Stankov. Phys. Rev. B **98**, *12*, 121409 (2018).
[8] E.P. Domashevskaya, A.A. Guda, A.V. Chernyshev, V.G. Sitnikov. Physics of the Solid State **59**, *2* 385 (2017).
[9] C. Blaauw, F. van der Woude, G.A. Sawatzky. J. Physics C **6**, *14*, 2371 (1973).
[10] R. Girlanda, E. Piparo, A. Balzarotti. J. Appl. Phys. **76**, *5*, 2837 (1994).
[11] I. Sandalov, N. Zamkova, V. Zhandun, I. Tarasov, S. Varnakov, I. Yakovlev, L. Solovyov, S. Ovchinnikov. Phys. Rev. B **92**, *20*, 205129 (2015).
[12] S. Eisebitt, J.-E. Rubensson, M. Nicodemus, T. Böske, S. Blügel, W. Eberhardt, K. Radermacher, S. Mantl, G. Bihlmayer. Phys. Rev. B **50**, *24*, 18330 (1994).
[13] S.J. Clark, H.M. Al-Allak, S. Brand, R.A. Abram. Phys. Rev. B **58**, *16*, 10389 (1998).
[14] H. Lange. Thin Solid Films **381**, *2*, 171 (2001).

[15] L.P. Peng, A.L. He. Mod. Numer. Simulat. Mater. Sci. **3**, *01*, 13 (2013).
[16] T. Pandey, D.J. Singh, D. Parker, A.K. Singh. J. Appl. Phys. **114**, *15*, 153704 (2013).
[17] Q.L. Qiu, J.J. Yuan, H.J. Cao, Y.Y. Zhu. 3rd Int. Conf. Material, Mechanical and Manufacturing Engineering (IC3ME 2015). Atlantis Press (2015). P. 1560.
[18] Materials Project. https://materialsproject.org/materials/mp-1714
[19] Materials Project. https://materialsproject.org/materials/mp-20738
[20] A.A. Guda, S.A. Guda, A. Martini, A.N. Kravtsova, A. Algasov, A. Bugaev, S.P. Kubrin, L.V. Guda, P. Šot, J.A. van Bokhoven, C. Copéret, A.V. Soldatov. npj Comput. Mater. **7**, *1*, 1 (2021)
[21] K. Schwarz, P. Blaha, G.K.H. Madsen. Comp. Phys. Commun. **147**, *1–2*, 71 (2002).
[22] P. Blaha, K. Schwarz, F. Tran, R. Laskowski, G.K. Madsen, L.D. Marks. J. Chem. Phys. **152**, *7*, 014101 (2020).
[23] P. Blaha, D.J. Singh, P.I. Sorantin, K. Schwarz. Phys. Rev. B **46**, *3*, 1321 (1992).
[24] J.P. Perdew, K. Burke, M. Ernzerhof. Phys. Rev. Lett. **77**, *18*, 3865 (1996).
[25] G.P. Potudanskii, S.I. Kurganskii, E.P. Domashevskaya. Mater. Res. Exp. **6**, *11*, 1150g9 (2019).
[26] F. Tran, P. Blaha. Phys. Rev. Lett. **102**, *22*, 226401 (2009).
[27] I. Khan, I. Ahmad, H.R. Rahnamaye Aliabad, M. Maqbool. Mater. Today: Proceeding **2**, *10*, 5122 (2015).
[28] F. Margarido, M.O. Figueiredo. Mater. Sci. Eng. A **104**, 249 (1988).
[29] F. Weitzer, J.C. Schuster. J. Solid State Chem. **70**, *2*, 178 (1987).
[30] F.A. Sidorenko, P.V. Gel'd, L.B. Dubrovskayo. Refract. Trans. Met. Comp. 178 (1964).
[31] B.A. Aronsson. Acta Chem. Scandinavica **14**, *6*, 1414 (1960).
[32] M.D. Manyakin, S.I. Kurganskii, O.I. Dubrovskii, O.A. Chuvenkova, E.P. Domashevskaya, S.V. Ryabtsev, R. Ovsyannikov, E.V. Parinova, V. Sivakov, S.Yu. Turishchev. Mater. Sci. Semicond. Proc. **99**, 28 (2019).
[33] A. Kokalj. J. Mol. Graph. Mod. **17**, *3–4*, 176 (1999).
[34] W. Setyawan, S. Curtarolo. Computat. Mater. Sci. **49**, *2*, 299 (2010).
[35] S.I. Kurganskii, N.S. Pereslavtseva. Physics of the Solid State **44**, *4*, 704 (2002).
[36] Giannini, S. Lagomarsino, F. Scarinci, P. Castrucci. Phys. Rev. B **45**, *15*, 8822 (1992).
[37] K. Radermacher, O. Skeide, R. Carius, J. Klomfaß, S. Manti. MRS Online Proc. Library Archive **320**, 115 (1993).
[38] H. Lange. 5th Int. Conf. on Solid-State and Integrated Circuit Technology. Proceedings (Cat. No. 98EX105). Beijing, IEEE (1998). P. 247.
[39] F.F.H. Aragón, L. Villegas-Lelovsky, L. Cabral, M.P. Lima, A. Mesquita, J.A.H. Coaquira. Nanoscale Adv. **3**, *5*, 1484 (2021).
[40] A. Fernandez-Pañella, T. Ogitsu, K. Engelhorn, A.A. Correa, B. Barbrel, S. Hamel, D.G. Prendergast, D. Pemmaraju, M.A. Beckwith, L.J. Bae, J.W. Lee, B.I. Cho, P.A. Heimann, R.W. Falcone, Y. Ping. Phys. Rev. B **101**, *18*, 184309 (2020).
[41] G.B. Grad, E.R. González, J. Torres Díaz, E.V. Bonzi. J. Mater. Sci. Res. Rev. **1**, *3*, 1 (2018).
[42] B. Khanbabaee, B. Arezki, A. Biermanns, M. Cornejo, D. Hirsch, D. Lützenkirchen-Hecht, F. Frost, U. Pietsch. Thin Solid Films **527**, 349 (2013).
[43] I. Akai, K. Iwamitsu, Y. Igarashi, M. Okada, H. Setoyama, T. Okajima, Y. Hirai. J. Phys. Soc. Jpn. **87**, *7*, 074003 (2018).
[44] E.V. Khramov, V.V. Privezentsev, A.N. Palagushkin. Poverknost. Journal of Surface Investigation: X-ray, Synchrotron and Neutron Techniques **14**, *6*, 1133 (2020).